PHOTONICS Research

Giant two-photon absorption of anatase TiO_2 in Au/TiO_2 core-shell nanoparticles

Lijie Wang,[1,3] Tsz Him Chow,[2] Malte Oppermann,[1,4] Jianfang Wang,[2] and Majed Chergui[1,*]

[1]Laboratory of Ultrafast Spectroscopy, ISIC and Lausanne Centre for Ultrafast Science (LACUS), École Polytechnique Fédérale de Lausanne (EPFL), CH-1015 Lausanne, Switzerland
[2]Department of Physics, The Chinese University of Hong Kong, Shatin, Hong Kong SAR, China
[3]Present address: Division of Physical Science and Engineering, King Abdullah University of Science and Technology (KAUST), Thuwal, Kingdom of Saudi Arabia
[4]Present address: Chemistry Department, University of Basel, 4001 Basel, Switzerland
*Corresponding author: majed.chergui@epfl.ch

Received 15 February 2023; revised 20 May 2023; accepted 21 May 2023; posted 24 May 2023 (Doc. ID 487784); published 28 June 2023

We report on deep-to-near-UV transient absorption spectra of core-shell Au/SiO_2 and Au/TiO_2 nanoparticles (NPs) excited at the surface plasmon resonance of the Au core, and of UV-excited bare anatase TiO_2 NPs. The bleaching of the first excitonic transition of anatase TiO_2 at ∼3.8 eV is a signature of the presence of electrons/holes in the conduction band (CB)/valence band (VB) of the material. We find that while in bare anatase TiO_2 NPs, two-photon excitation does not occur up to the highest used fluences (1.34 mJ/cm^2), it takes place in the TiO_2 shell at moderate fluences (0.18 mJ/cm^2) in Au/TiO_2 core-shell NPs, as a result of an enhancement due to the plasmon resonance. We estimate the enhancement factor to be of the order of ∼10^8–10^9. Remarkably, we observe that the bleach of the 3.8 eV band of TiO_2 lives significantly longer than in bare TiO_2, suggesting that the excess electrons/holes in the conduction/valence band are stored longer in this material.

https://doi.org/10.1364/PRJ.487784

1. INTRODUCTION

Transition metal oxides (TMOs) have been attracting growing interest as candidates for nonlinear (NL) optical materials, due to their high optical nonlinearities, ultrafast response times, and low absorption indices [1,2]. TMOs are also the prime candidates for transparent conductive oxides (TCOs), because of their large bandgap and transparent and conducting properties, whose films are utilized in flat panel displays [3], solar cells [4], and electroluminescent devices as transparent electrodes [5].

Being one of the most commonly investigated TMOs, TiO_2 in its various polymorphs (anatase, rutile, and amorphous) also possesses remarkable properties, such as the high stability of its excitonic transitions to perturbations such as defects, temperature [6], and excess charge doping [7]. For all optical switching applications, anatase TiO_2 thin films exhibit an interesting fast and reasonably large NL optical response at 800 nm [1]. It was, however, noted that the physical properties and, thus, the NL optical response of TiO_2 films are strongly dependent on the processing route [8], as well as on the inclusion of metallic nanoparticles (NPs) [9,10].

Measurements of the NL optical properties of TiO_2 polymer nanocomposites demonstrated negligible two-photon absorption (TPA) and a negative value of the NL refractive index [11]. This is in line with reports showing no TPA of anatase TiO_2 NPs in solution even up to fluences of 300 mJ/cm^2 [12,13]. On the other hand, large second- and third-order optical nonlinearities of the Au/TiO_2 composite films were observed and attributed to the high density of Au particles in nonconductive films, and the strong local field enhancement caused by the localized surface plasmon resonance (LSPR) absorption [14]. In particular, it was reported that Au/TiO_2 composites can exhibit a self-defocusing and saturating nonlinearity at optical intensities up to 5.6 GW/cm^2, while measurements on a pure TiO_2 film did not show any nonlinearity [15].

Stable core-shell Au/TiO_2 and Ag/TiO_2 NPs were reported to exhibit saturable absorption or optical limiting at 532 nm nanosecond-pulse excitation, depending on the applied laser fluence [16]. This behavior was explained in terms of the electronic Kerr nonlinearities and NL scattering in the NPs. The samples were subject to laser fluences up to 20 J/cm^2 and powers up to 2.8 GW/cm^2, and showed no appreciable signs of laser-induced damage, making them promising candidates for high energy optical limiting [16]. It has also been noted that Au NP-doped multilayers such as Au/SiO_2 and Au/TiO_2 films can be used as optical filters, due to their high damage threshold and their larger third-order NL susceptibilities.

It has been established that excitation of the LSPR band of Au NPs deposited on or embedded in TiO_2 films leads to injection of electrons from the Au NP into TiO_2 [17–23]. Just as for dye-sensitized NPs, probing and time-resolving the electron injection from molecular dyes into TiO_2 was performed using visible-to-THz probes [18,21,23,24], X-ray absorption spectroscopy (XAS) at the Ti K-edge [12,25,26], and, more recently, X-ray photoelectron spectroscopy sensitive to the Au 4f- and Ti 2p-orbitals [27]. Overall, the optical-domain pump-probe studies concluded that electron injection is prompt, within the cross correlation of the experiments (typ. <200 fs), and takes place with an efficiency reaching 40%–50% [18,23]. It should be stressed that these time-resolved experiments concerned Au NPs deposited on TiO_2 surfaces [18,24,27] or embedded in TiO_2 films [23], and were all carried out in the linear regime of pump-pulse intensity.

Thus, it appears that the Au NPs can influence the optical properties of the Au/TiO_2 system in different ways: electron injection and/or enhanced NL effects (e.g. TPA, saturable absorption) due to the presence of the plasmon field. To weigh these various contributions, it is important to have simultaneously spectroscopic fingerprints of the presence of electrons in the conduction band (CB) of TiO_2 and of the Au NP transitions, as well as their temporal evolutions. This has not been the case in any of the above-mentioned studies reporting TPA in Au/TiO_2 composite materials.

In recent years, Baldini *et al.* [6,13,28] carried out a thorough investigation of the spectroscopy and charge carrier dynamics of bare anatase TiO_2 NPs using pump-probe spectroscopy in the deep-ultraviolet (3.3–4.6 eV). In particular, they identified the first excitonic transition of the system at ~3.8 eV and showed that it could be used as a marker of electron injection in dye-sensitized TiO_2 NPs, by detecting its bleaching due to the blocking of the transition that results from the excess of electrons/holes in the CB/valence band (VB). Further to this, Wang *et al.* [29–31] used the same tools to investigate the spectroscopy and charge carrier cooling in Au NPs. The novelty of the latter work lies in the fact that they probed the region of interband transitions of the Au NPs for the first time. Thus, in the present case, the deep-UV probe offers the advantage that the characteristic transitions of both the Au core and the TiO_2 shell fall in the same spectral region, so that their behavior can be simultaneously monitored.

Here we investigate the response of Au/TiO_2 NPs in aqueous solution using pump-probe TA spectroscopy upon resonant excitation of the LSPR of the Au NP core in the visible, while the probing is done using the deep-UV broadband continuum. By detecting the excitonic transition of anatase TiO_2 when excessive electrons/holes are present in the CB/VB [13], we get insights into the excitation mechanism of the system. We compare these results with LSPR-excited core-shell Au/SiO_2 NPs and above the bandgap (BG) excited bare TiO_2 NPs. The BG of SiO_2 is too large (7.5 to 9.6 eV) for any electron injection from the excited Au core to take place, or it would require absorption by three to four visible photons, which is a very low-probability event. We observe that at pump energies resonant with the LSPR of the Au core, efficient TPA of anatase TiO_2 promotes electrons from the VB directly into the CB by simultaneously absorbing two green photons. Even at higher pump fluences, no TPA is observed in the case of bare TiO_2. We also find that the excess electrons/holes generated in the CB/VB have a significantly longer lifetime than in bare TiO_2, offering a strategy to store charges. The experimental setup and procedures are presented in the appendix.

2. RESULTS AND DISCUSSION

Figure 1 shows the absorption spectra of bare anatase TiO_2 and bare Au NPs, as well as core-shell Au/SiO_2 and Au/TiO_2 NPs; the inset zooms into the region of the LSPR band of Au/SiO_2 and Au/TiO_2 NPs. The bare anatase TiO_2 NP shows the well-known absorption with a wing extending down to ~3 eV, due to scattering. The shoulder at ~3.8 eV corresponds to the first excitonic transition of anatase TiO_2, as previously discussed in detail [6]. The spectra of ~25-nm-diameter bare Au and Au/SiO_2 NPs are almost identical with both exhibiting the LSPR band at ~2.35 eV, and at higher energies, the region of interband transitions, discussed in Refs. [29,30]. In the case of Au/TiO_2 core-shell NPs, the LSPR band shifts to the red by ~0.37 eV and exhibits a red wing extending down to ~1.5 eV spectrum. Its spectrum is similar to that of ~10-nm-diameter Au NPs embedded in a TiO_2 film [23]. The red shift of the LSPR in Au/TiO_2 compared to Au/SiO_2 is fully accounted for by the dielectric effects [23,32].

Figure 2 shows the time-energy deep-UV transient absorption (TA) maps and the corresponding TA spectra at different time delays of the three samples: bare anatase TiO_2 NPs excited at 4.0 eV above the BG, and Au/SiO_2 and Au/TiO_2 core-shell NPs excited into the Au LSPR band at 2.0–2.4 eV. The TA of bare anatase TiO_2 NPs [Fig. 2(a)] is identical to what was reported in Refs. [6,28]. The TA spectra of bare anatase TiO_2 at 1, 100, and 800 ps time delay [Fig. 2(b)] clearly exhibit a negative (bleach) signal over the entire probe range with a band centered at ~3.83 eV, which represents the first excitonic transition of anatase TiO_2 [6]. The bleach signal is due to

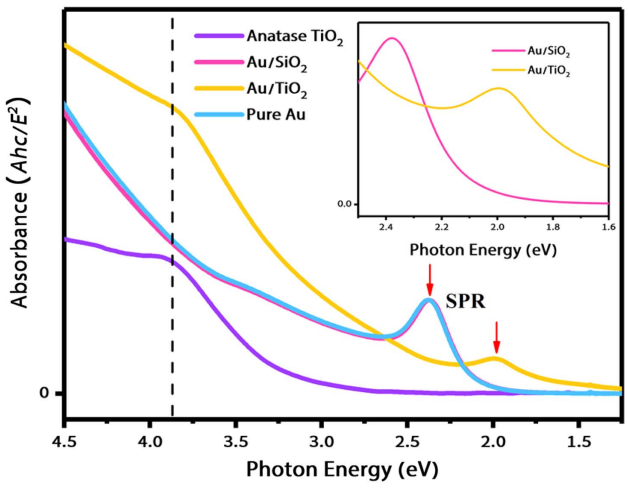

Fig. 1. Steady-state absorption spectra of the samples investigated in this work. The two pink arrows show the LSPR peaks of Au/SiO_2 and Au/TiO_2 NPs, respectively, and the inset zooms into the LSPR part of the Au/SiO_2 and Au/TiO_2 NPs; all NPs are dispersed in aqueous solution.

electrons/holes generated by BG excitation into the CB/VB of TiO_2. Figure 2(c) shows the TA map for Au/SiO_2 NPs excited with a broadband pulse (2–2.4 eV) at the LSPR, and Fig. 2(d) shows the TA spectra. These results are close to those we recently reported for the case of bare Au NPs of identical size [29,30]. The TA maps and spectra for Au/SiO_2 NPs exhibit three main features: two negative ones at ~3.8 eV and ~4.4 eV, and a positive one at ~3.4 eV. Briefly, they were identified in Refs. [29,30] using the band structure diagram of bulk Au, as interband transitions from the 5d valence band to the 6sp band above the Fermi level at the *X* and *L* symmetry points for the two negative ones, monitoring the population of electrons and holes, above and below the Fermi level, respectively. The positive band was identified as a transition between valence sub-bands (i.e. an intraband transition), monitoring the population of holes. The overall conclusion was that charge carrier cooling is slow (~150 ps) and commensurate with the time scale of thermal lattice cooling (~250 ps). The fluence

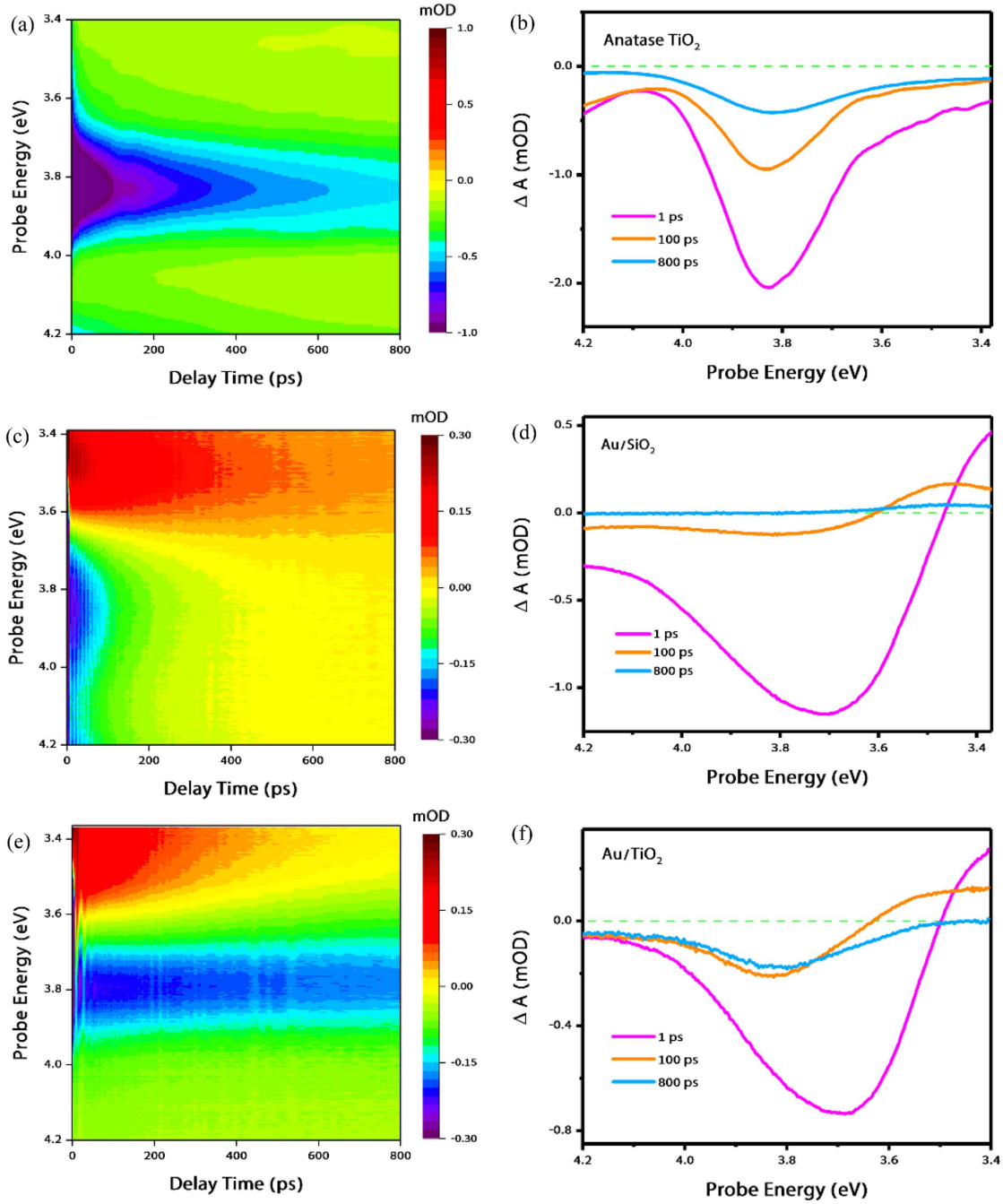

Fig. 2. Time-energy TA maps and the corresponding spectral traces at 1, 100, and 800 ps. (a), (b) Bare anatase TiO_2 NPs upon above-BG excitation (4.0 eV); (c), (d) Au/SiO_2 NPs upon plasmon excitation (2.0–2.4 eV); (e), (f) Au/TiO_2 NPs upon plasmon excitation (2.0–2.4 eV) with a fluence of ~330 μJ/cm^2; all NPs are dispersed in aqueous solution.

dependence of the 3.4 and 3.8 eV bands at a time delay of 50 ps is shown in Fig. 3, and it clearly reflects a one-photon excitation process.

Figures 2(e) and 2(f) show the TA maps and spectra for the Au/TiO_2 NPs excited by a 2.0–2.4 eV broadband pulse. Compared to Figs. 2(c) and 2(d), some notable differences but also similarities arise. First, the ∼3.4 eV positive signal (due to holes in the Au core) is shorter-lived in Au/TiO_2. Second, a band shows up centered at ∼3.8 eV (the early time signal at this band is due to the Au NP, but it dramatically decays within ∼10 ps, as observed in the Au/SiO_2 case). Thereafter, the bleach signal persists up to the longest time of our temporal window. Figure 4 compares the 800 ps transients for the three samples. For the Au/SiO_2 sample, the signal has all but died away, except for the weak remnant of the positive feature <3.6 eV. However, the signal for bare anatase TiO_2 and Au/TiO_2 NPs exhibits the same bleach feature at 3.8–3.83 eV. Given that the equivalent band due to the Au core has fully decayed, we conclude that this is the bleach due to electrons/holes in the CB/VB of the TiO_2 shell in Au/TiO_2 NPs [13,28]. This is further supported by Fig. 5, which shows the time profiles of the 3.8 and 3.4 eV bands for both core-shell NPs. Finally, the features >4.1 eV in Au/SiO_2 do not show up in the case of Au/TiO_2, due to the fact that the Au contribution to the transient is shaded by the strong absorption of TiO_2 in this region.

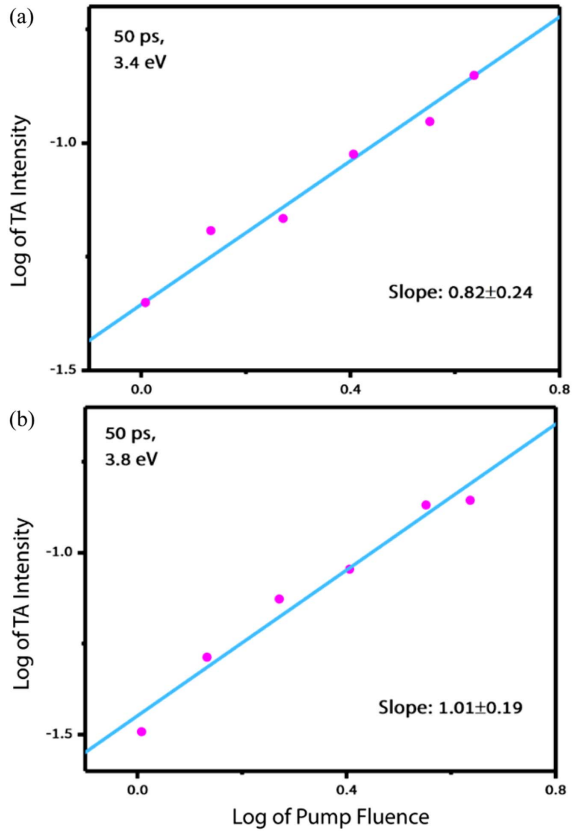

Fig. 3. Fluence dependence of the bands appearing in the plasmon-excited TA spectra of Au/SiO_2 NPs at 50 ps time delay, displayed as a log–log plot of TA intensity versus pump fluence: (a) 3.4 eV and (b) 3.8 eV.

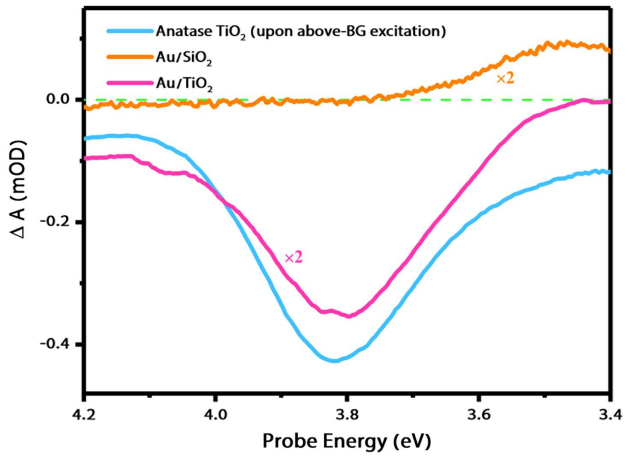

Fig. 4. Comparison of the TA spectra of the three measured samples (rescaled for clarity). The blue solid line is the transient response of bare anatase TiO_2 at a delay time of 800 ps upon UV excitation (above-BG excitation, 4.0 eV). The orange and red lines represent the TA spectra of Au/SiO_2 and Au/TiO_2 at a time delay of 800 ps upon plasmon excitation (below-BG excitation, 2.0–2.4 eV), with a fluence of ∼330 μJ/cm^2.

The main observation here is the long-lived bleach band in Au/TiO_2 NPs at the position (∼3.8 eV) of the first excitonic transition of anatase TiO_2. Excess electrons/holes in the CB/VB could either originate from the electrons transferred from the VB of TiO_2 or the injected electrons from Au NPs. The presence of the intraband transition of Au at ∼3.4 eV is indicative of holes in the Au NP core, due to electrons that have been removed from below the Fermi level upon LSPR excitation. They may end up in the CB of TiO_2 as expected in the scenario of plasmon-induced electron injection into the TiO_2 shell, typically within hundreds of femtoseconds [18,23]. However, the time scales of the band around ∼3.4 eV and ∼3.8 eV are not commensurate, implying that hole decay in the Au core is not due to a back-electron transfer from TiO_2, but rather by the kinetics of charge carrier cooling just as in Au/SiO_2 NPs [29,30]. Of course, the decay time of the 3.4 eV band is shorter here, which may point to an influence of the TiO_2 shell. This is not surprising considering the way the latter affects the spectral features of the Au core (Fig. 1). In summary, it appears that the ∼3.8 eV feature consists of three contributions: one at very early times, due to charge injection from the Au core; the second at early to somewhat later times due to the response of the Au interband transitions (close to that of Au/SiO_2 NPs); and a third one that persists up to the longest time delay, which is due to the bleached TiO_2 excitonic band.

Further insight into the origin of the population mechanisms in the CB of TiO_2 is given by the fluence dependence of the various bands at short (10 ps), intermediate (50 ps), and long (800 ps) time delays (see Appendix C). Figures 6(a)–6(c) show log–log plots of the signals of Au/TiO_2 at ∼3.8 eV at these time delays for pump fluences ranging from 0.16 to 0.98 mJ/cm^2. The slopes of the signal are 1.32 ± 0.20, 1.55 ± 0.66, and 1.83 ± 0.21 at 10, 50, and 800 ps time delay, respectively. While the latter points to a predominant

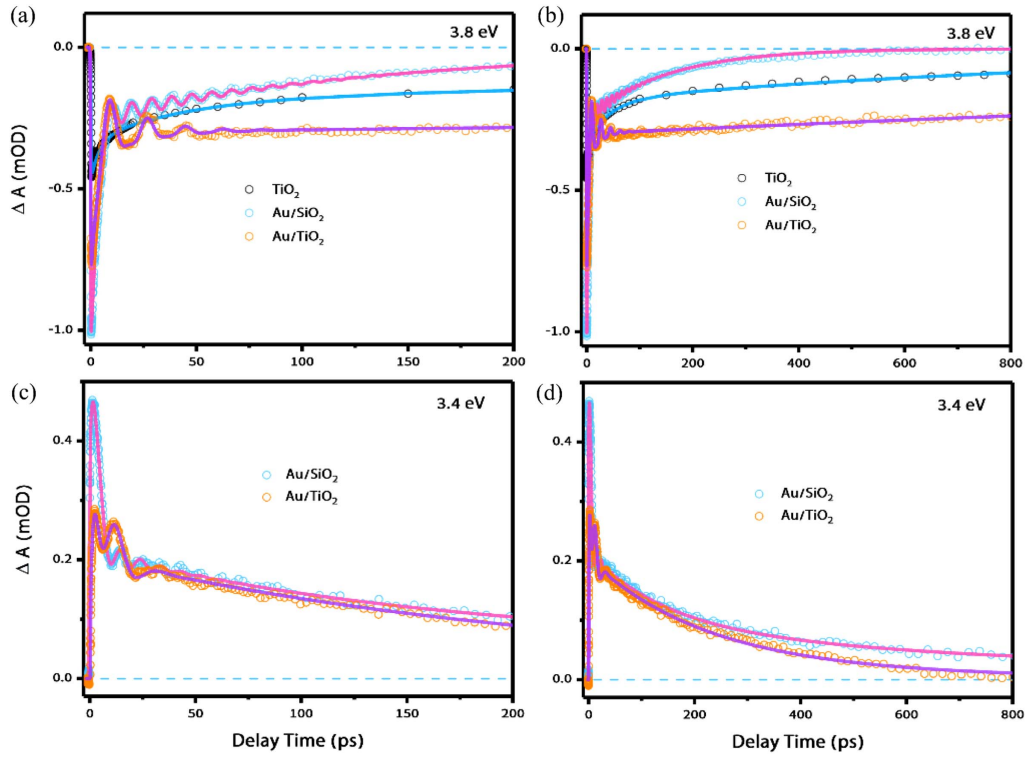

Fig. 5. Comparison of the TA time traces between Au/SiO_2 and Au/TiO_2 NPs at probe energies of (a), (b) 3.8 eV; (c), (d) 3.4 eV within (a), (c) 200 ps; (b), (d) 800 ps. The TiO_2 was excited above the BG, while the Au/SiO_2 and Au/TiO_2 were excited upon plasmon excitation, and all the samples are excited with a fluence of ~330 $\mu J/cm^2$. The blue and orange circles are experimental traces; the red and purple solid lines are the fitted time traces.

two-photon process, the former two point to a regime intermediate between one- and two-photon absorption. Further, these slopes reflect an increasing weight of the TPA-induced signal as a function of time. This can be rationalized by noting that the ~3.8 eV signal contains the contributions of the interband transition of the Au NP, the electron injected via LSPR excitation, and the excitonic transition of anatase TiO_2. As already mentioned, the first contribution, which dies away in ~250 ps, has a linear dependence on the pump fluence (Fig. 3). The second contribution, also linear with pump fluence, dies away much faster (<50 ps) according to Refs. [23,27]. Therefore, at 10 and 50 ps delays, it is present [as seen in Figs. 2(c) and 2(d)], while at 800 ps it has vanished. In the latter case, we are left with a predominant TPA contribution that involves the TiO_2 shell. This process is of course present from the earliest times onwards but is overlapped by the above one-photon contributions. Figure 7 shows the value of the ~3.8 eV signal slope as a function of time. We assume a maximum value of 2 at infinite times, considering that all signals due to the Au core have died away. The biexponential fit of the data point yields values of $\tau_1 \approx 50$ ps and $\tau_2 > 2$ ns with uncertainties of a factor of 2. Bearing in mind the latter, it is fair to say that the first component decays on comparable time scales to its counterpart in Au/SiO_2 NPs, as is actually the case with the 3.4 eV band [Figs. 2(c) and 2(d)].

Finally, the fact that three contributions are at play is visible from Fig. 8, which shows the change of profile of the TA spectra at 10 ps time delay for increasing fluences under visible (2.0–2.4 eV) excitation. Whilst for Au/SiO_2 the TA profile does not change with pump fluence [Fig. 8(b)], for Au/TiO_2 clear changes are observed with the growth of a blue shifted bleach band implying that the TPA-induced TiO_2 excitonic bleach is taking over the overall bleach contribution with increasing pump power [Fig. 8(c)]. Note that for bare TiO_2, there is no effect on the TA spectra over the same range of fluences, implying no signal indicative of charge carriers in the VB/CB. To further make the point about the two-photon process causing the bleach of the 3.8 eV band, Fig. 9 shows the log–log plots of the signal due to the ~3.4 eV band of Au/TiO_2 NPs at 10 ps and 50 ps, respectively. Its slope is close to 1 (bearing in mind the large error bars), which is reasonable since this band is due to holes in the Au core caused by the LSPR excitation [29]. Note that the 3.4 eV band is at the limit of our detection, and therefore its signal at 50 ps is weak, which explains the relatively large uncertainty of its slope.

Coming back to the ~3.8 eV signal, one may ask whether the early time one-photon absorption signal could be due to injection of electrons from the Au core [18,21,33], which then decay on a ~250 ps time scale. This might be excluded because: first, it is not supported by the shape of the transients in Fig. 8(b); second, its decay is comparable to what was reported for the same band in Au/SiO_2 NPs [29,30]; and, third, as was shown by Ratchford *et al.* [23] in the case of Au NPs embedded in TiO_2 films, the injected electrons have a fast

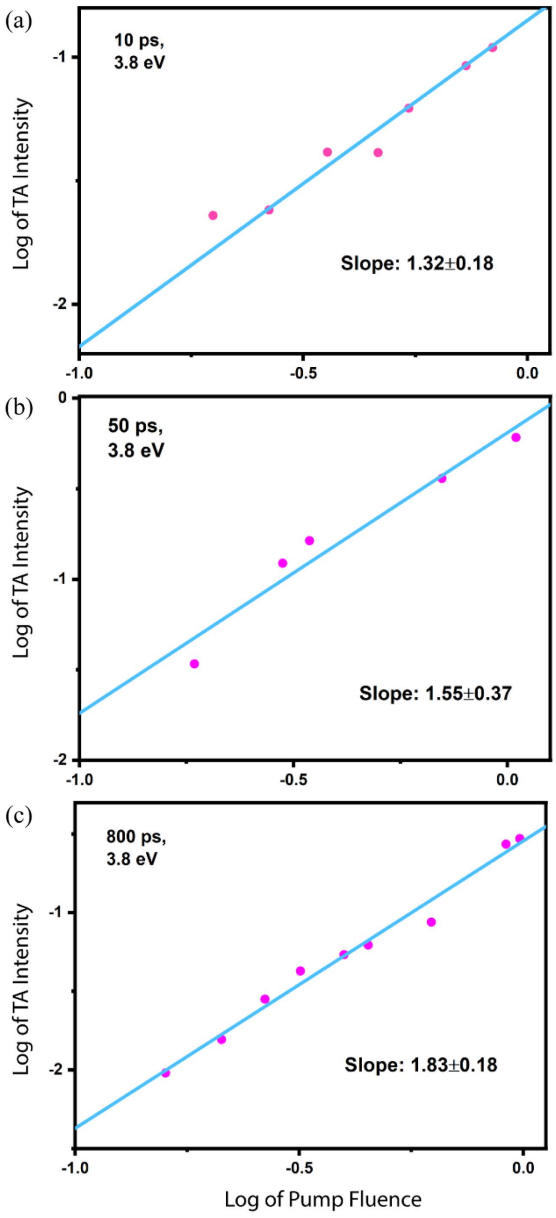

Fig. 6. Fluence dependence of the 3.8 eV band of TA spectra of Au/TiO_2 NPs excited at the LSPR of the Au core, displayed as a log–log plot of TA intensity versus pump fluence, which varies in a range from 0.16 to 0.98 mJ/cm^2: (a) 10 ps, (b) 50 ps, and (c) 800 ps. At 800 ps, the positive contribution due to the Au has died away. The magenta dots are the experimental values, and the solid cyan lines represent their fits with a linear function.

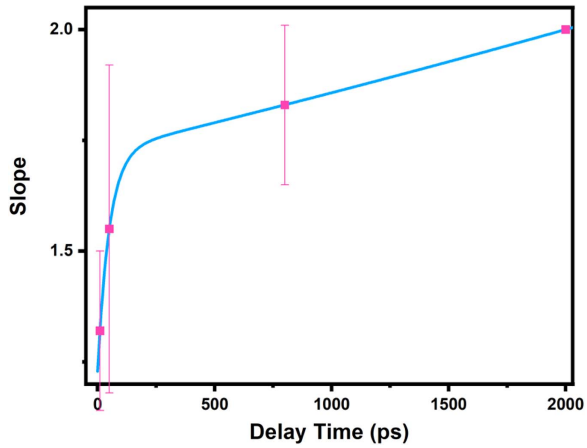

Fig. 7. Time dependence of the slopes of the fluence dependence of the Au/TiO_2 NPs at 3.8 eV. The solid line relates to the fit using the biexponential model with time constants of $\tau_1 = 49.5$ ps and $\tau_2 > 2000$ ps.

decay (~2 ps) followed by a long-lived (on the window of 20 ps of their time scan) weak component. We can therefore conclude that the early time signal is largely due to the response of the Au core. This does not exclude a TiO_2 response due to injected electrons, but their contribution is short-lived. The bleach signal at 800 ps time delay, when the signal of the Au core has died away, is therefore due to the TiO_2 excitonic bleach only. Its slope of 1 .83 ± 0.21 reflects the fact that the electrons/holes in the CB/VB of TiO_2 have been generated via a TPA process. Again, we stress that the same range of fluences does not show any signal in bare TiO_2 NPs, which would be due to electrons/holes in the CB/VB [Fig. 8(a)]. This is in line with previous studies, which used fluences up to 200 mJ/cm^2 of a 10 ps/532 nm laser [12], i.e., two orders of magnitude larger than in the present case, showing no evidence of two-photon excitation. In Ref. [13], femtosecond pulse excitation at either 400 nm or 550 nm with fluences up to 53 mJ/cm^2 also showed no sign of multiphoton excitation. On the other hand, in the case of dye-sensitized TiO_2 NP, the fluence dependence of the ~3.8 eV band due to injected electrons remained in the linear regime up to 336 $\mu J/cm^2$ using 550 nm excitation. These observations lead us to conclude that the occurrence of multiphoton excitation of TiO_2 in Au/TiO_2 core-shell NPs is due to the presence of the Au core and is mediated by the resonance excitation of its LSPR.

We estimated the enhancement factor of the TPA of TiO_2 in Au/TiO_2 NPs, as described in Appendix D. Based on our experimental TA intensity (we took an average ΔA value of ~0.3 at 3.8 eV, over the 10–200 ps range), from Fig. 2(e), we calculate that in Au/TiO_2 NPs, the enhancement factor of the third-order NL two-photon process is $\sim 10^8$–10^9. This is consistent with the results of surface-enhanced Raman scattering (SERS) [34,35] utilizing LSPR of nanostructured metallic NPs (e.g. Au, Ag, Cu) to amplify Raman signals of molecules at their surface with enhancement factors of 10^6–10^{11}. It is also reported that the quantum yield of fluorescence in Au nanorods compared to a bulk metal surface is enhanced by a factor of more than 1 million [36,37]. In addition, simulations show that the enhancement of the molecular TPA cross section by the LSPR may reach many orders of magnitude, depending on the distance of the NPs and the $|E|^4$ local field [38,39].

This huge enhancement of the TPA cross section in the case of core-shell Au/TiO_2 NPs should be contrasted to the linear dependence reported in the case of Au NP charge injection into anatase TiO_2 [17–23]. This suggests that the architecture of NPs deposited on the surface of TiO_2 does not favor LSPR enhancement of TPA, which is likely caused by the

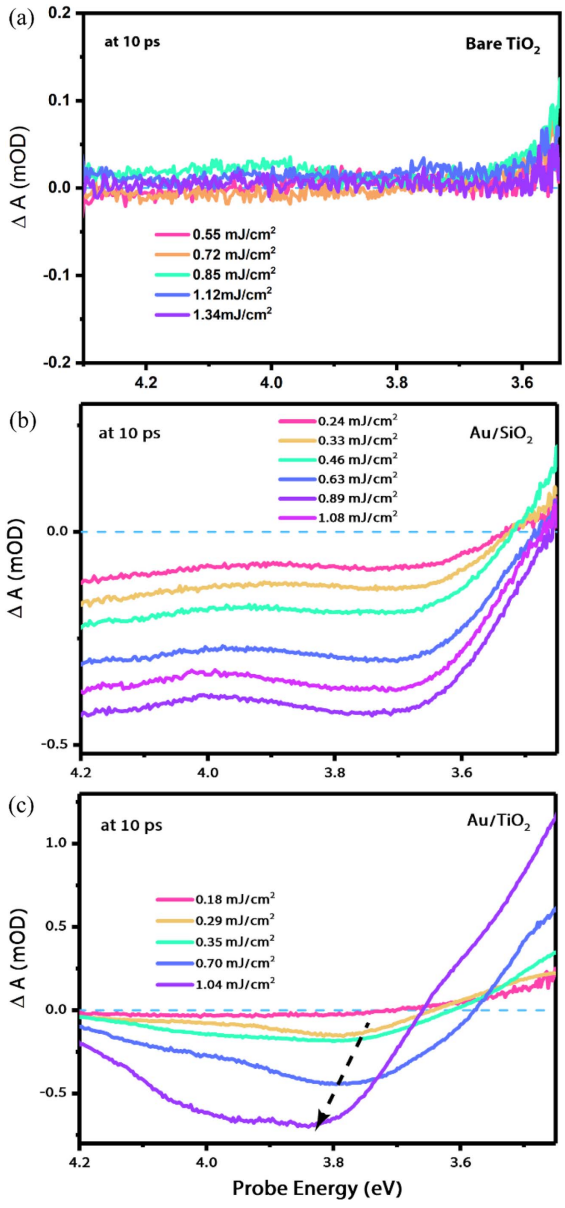

Fig. 8. TA spectra at 10 ps of (a) bare TiO_2 NPs, (b) Au/SiO_2, and (c) Au/TiO_2. All samples are excited at the plasmon resonance (2.0–2.4 eV) for different values of the fluence.

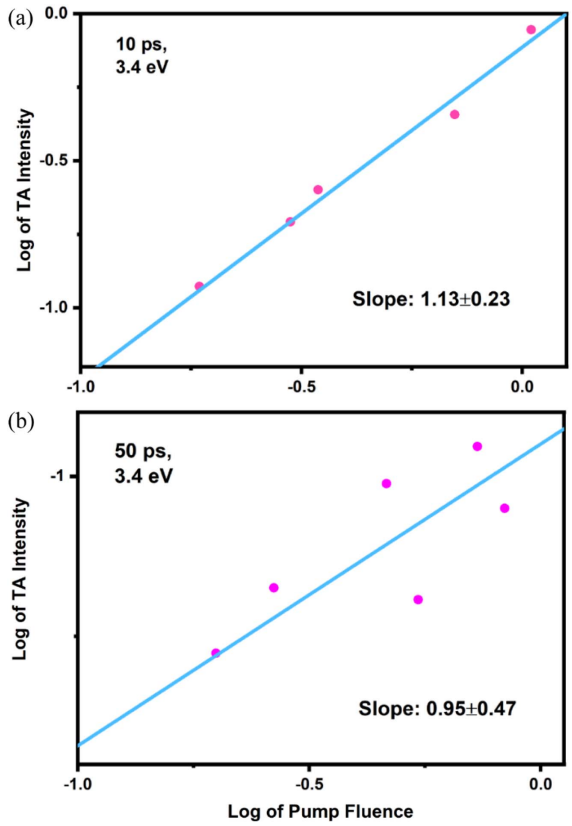

Fig. 9. Fluence dependence of the Au/TiO_2 NPs at 3.4 eV, displayed as a log–log plot of TA intensity versus pump fluence, which varies in a range from 0.16 to 0.98 mJ/cm^2: (a) at 10 ps and (b) at 50 ps.

limited contact interface with the NP in this architecture [18,24,27]. The case of Au NP embedded in the TiO_2 film [23] is close to the core-shell architecture (although the Au NPs are densely stacked), but the upper fluence used in their work is close to the lowest in ours. It is also interesting to note that while on the short time scale (<20 ps), the decay of the signal due to injected electrons is faster in the Au/TiO_2, but leaves a weak long component, we observe that for the long time case, the excitonic bleach survives for significantly longer time than in bare TiO_2 NPs [Fig. 5(b)]. The short time decay is probably due to injected electrons that go back to the Au NP, as also suggested by Borgwardt *et al.* [27], while the long-time component in their work may correspond to the one we observe here.

3. CONCLUSION

This paper reports on two remarkable observations: first, TPA in TiO_2 occurs, and is initiated already at mild fluences; and, second, a longer-lived excitonic bleach of TiO_2 compared to the bare NPs, implying that the presence of the Au core "blocks" the electron–hole recombination in the TiO_2 shell. It is not clear what mechanism could be behind this behavior, as the charge carrier dynamics in the Au core is over, while the bleach of the excitonic band goes on up to the time limit of our detection. Nevertheless, that electrons/holes in the CB/VB are present for a long time deserves further investigation as it opens perspectives in terms of charge storage in a TMO, with possible applications in the field of TCO and photocatalysis.

APPENDIX A: SAMPLE PREPARATION

Growth of the Au NPs: The Au NPs samples were synthesized through a seed-mediated growth method by a previously reported procedure [40]. Specifically, a cetyltrimethylammonium bromide (CTAB solution) (0.1 M, 9.75 mL; 1 M = 1 mol/L) was first mixed with a $HAuCl_4$ solution (0.01 M, 0.25 mL), followed by the rapid injection of a freshly prepared, ice-cold $NaBH_4$ solution (0.01 M, 0.60 mL) under vigorous stirring. The resultant solution was kept under gentle stirring for 3 h

at room temperature. 0.24 mL of the as-prepared seed solution was injected into a growth solution made of CTAB (0.1 M, 19.5 mL), water (380 mL), $HAuCl_4$ (0.01 M, 8 mL), and ascorbic acid (0.1 M, 30 mL) afterwards. The reaction mixture was gently mixed well and left undisturbed overnight at room temperature. The resultant Au NPs sample were washed and concentrated three times into water by centrifugation and redispersion for further use.

Preparation of the silica coated Au NPs: CTAB molecules adsorbed on Au NPs were first replaced by thiol-terminated methoxy poly(ethylene glycol) (mPEG–SH). Au NP solution (100 mL) was centrifuged and redispersed in water (20 mL). Then, mPEG–SH (polymer chain concentration 1 mM) solution (2 mL) was subsequently added. The resultant solution was kept undisturbed at 25°C for 12 h and then centrifuged twice to remove the excess mPEG–SH polymers. The obtained mPEG-coated Au NPs were redispersed in a solution mixture containing 4.5 mL of water, 15 mL of absolute ethanol, and 0.3 mL of $NH_3 \cdot H_2O$ (30% in mass fraction). After that, 0.08 mL of the silica precursor solution [5% (volume fraction) tetraethylorthosilicate (TEOS) in absolute ethanol] was injected into the Au NP solution under ice-cold and ultrasonication conditions for 1.5 h.

Preparation of the titania-coated Au NPs: The preparation of titania-coated Au NPs (Au/TiO_2 NPs) was a modified synthetic procedure [41]. $TiCl_3$ was used as the TiO_2 precursor. The CTAB-capped Au NPs were first wrapped with poly(sodium 4-styrenesulfonate) (PSS). Typically, the solution (20 mL) of an as-grown CTAB-capped Au NP sample was first centrifuged to remove the excess surfactant and then redispersed into water (10 mL). The resultant Au NP solution was then added dropwise under vigorous stirring to an aqueous PSS solution (10 mL, 2 $g \cdot L^{-1}$, containing 6 mM NaCl). PSS adsorption was allowed for at least 6 h at room temperature. After the excess PSS was removed by centrifugation, the PSS-encapsulated Au NPs were redispersed into water (0.2 mL). $TiCl_3$ solution [0.2 mL, 17.1% (mass fraction), containing 25% (mass fraction) HCl] and water (6 mL) were first added into a glass bottle. $NaHCO_3$ solution (0.93 M, 1.1 mL) was then dropped, followed by the immediate addition of the PSS-encapsulated Au NP solution under stirring. After the mixture solution was stirred for 30 min at room temperature, the product was washed by centrifugation twice and redispersed in water (10 mL) before further use. To prepare anatase-phase titania-coated Au NPs, the thermal treatment of the washed and completely dried Au/TiO_2 nanostructures was carried out in a box furnace in air at 450°C for 2 h with a ramp rate of 5 $K \cdot min^{-1}$.

Figures 10(a)–10(c) show representative transmission electron microscopy (TEM) images of the pure Au, Au/SiO_2, and Au/TiO_2 NPs, which were synthesized by growing TiO_2 or SiO_2 shell on pregrown Au NPs mentioned above. They show well-defined core-shell nanostructures with a clear boundary between the Au core and the TiO_2/SiO_2 shells. This also reflects the excellent quality of the contact interface. The total size of the $Au/SiO_2/Au/TiO_2$ is ~65 nm in diameter with a ~25-nm-diameter Au core and ~20-nm-thick TiO_2 shell, and all NPs are dispersed in aqueous solution.

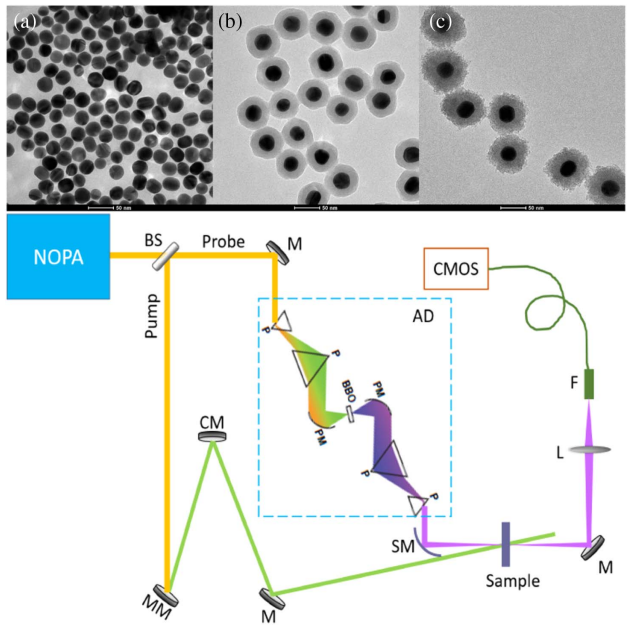

Fig. 10. Transmission electron microscopy images of (a) pure Au NPs, (b) Au/SiO_2 NPs, and (c) Au/TiO_2 NPs. Below is a diagram of the ultrafast broadband deep-to-near-UV spectroscopy setup, detailing the broadband pump-probe experiment after the noncollinear optical parametric amplifier. The blue dashed box shows the schematic of the achromatic doubling, adapted from Ref. [43]: BS, beam splitter; M, mirror; MM, multilayer mirror; CM, chirped mirror; SM, spherical mirror; PM, off-axis parabolic mirror; P, prism; L, lens; F, multimode fiber.

APPENDIX B: EXPERIMENTAL PROCEDURES AND METHODS

The experiments were performed using a pump-probe setup allowing for broadband deep-to-near-UV TA upon visible excitation of the samples [42,43]. A 20 kHz Ti:sapphire regenerative amplifier (KMLabs, Wyvern500) providing 50 fs/0.6 mJ pulses at 800 nm, pumps a non-colinear optical parametric amplifier (NOPA) to generate sub-90-fs visible pulses of 13 μJ/pulse in the 510–740 nm (1.68–2.43 eV) range. About 60% of the output is used as the pump pulses, which are spectrally filtered via several reflections of multilayer mirrors to give a green pump beam (2.0–2.4 eV). The pump pulses are further compressed by chirp mirrors to deliver <20 fs duration. The remaining 40% NOPA output is used to generate broadband UV probe pulses with ~100 nm bandwidth through an achromatic doubling scheme [44]. The schematic representation of the probe configuration is shown in Fig. 10. A half-wave plate is used to set the relative polarization between the pump and probe at the magic angle (54.74°) to avoid photo-selection effects. The laser beam spot sizes of the pump and probe are ~120 μm and ~50 μm full widths at half maximum (FWHMs), respectively. In all measurements, the pump fluence has ~10% uncertainty due to the laser power measurement and beam spot size. The sample is in a 0.2-mm-thick quartz drilled-flow cell and rotated by an electric motor to prevent photo-damage.

The morphology of the samples was observed by TEM (FEI Tecnai Spirit microscope operating at 120 kV). The

steady-state absorption spectra were recorded at room temperature using a commercial UV-Vis spectrometer (Shimadzu, UV-3600), and a reference spectrum of the pure solvent (water) was recorded for the baseline correction before measuring the absorption spectrum. To convert the nm to eV scale, we followed the Jacobian conversion method [45]. The wavelength is converted to energy using $E = hc/\lambda$, and the signal values themselves must be scaled by hc/E^2, where E represents the photon energy, h is the Planck constant, c is the light speed, and λ represents the wavelength.

The instrument response function (IRF) was determined by measuring the FWHM of the cross-phase modulation (CPM) at time zero of the pure water solvent (in a 0.2 mm optical path length drilled-flow cell). We adopted a procedure by fitting the CPM signal with a function composed of a Gaussian and its first and second derivatives as below [46]:

$$G(t) = \frac{1}{\sigma\sqrt{2\pi}}\exp\left(-\frac{t^2}{2\sigma^2}\right), \tag{B1}$$

$$G(t)' = \frac{c-t}{\sigma^3\sqrt{2\pi}}\exp\left(-\frac{(t-c)^2}{2\sigma^2}\right), \tag{B2}$$

$$G(t)'' = \frac{t^2-2ct-\sigma^2+t^2}{\sigma^5\sqrt{2\pi}}\exp\left(-\frac{(t-c)^2}{2\sigma^2}\right), \tag{B3}$$

of which the FWHM $= 2\sigma\sqrt{2\ln(2)}$, t is the time variable, and c is the offset of time zero. The IRF was found to be ~250 fs.

APPENDIX C: FLUENCE-DEPENDENCE MEASUREMENT AND CORRECTION OF THE EXCITATION INTENSITY

The fluence-dependence experiments were performed on the same deep-UV TA setup, measuring the TA at specific time delays between pump and probe, in a range of pump fluences.

Prior to the measurement, we first determine the time zero position at the delay stage, by looking at the point where the signal starts to appear while electronically moving the stage. Second, we convert the desired delay time into distance on the stage, and calculate the position of the stage with respect to time zero. Then we set two time points slightly before and after the desired time (e.g., it measures TA response at ~9.9 ps and ~10.1 ps if 10 ps is chosen) and take the average TA values at these two time points.

The average incident laser fluence F (measured in mJ/cm^2) is defined as $F = P/(r \cdot A)$, where P is the average laser power, r is the repetition rate of the laser system, and A is the laser beam spot size. The measurement of the laser beam spot size is performed using a camera-based beam profiling system consisting of a camera and analysis software, and the spot diameter is determined by the FWHM of the beam profile. We first set a range of the pump power (the upper power limit is determined by the laser system, and the lower limit is selected based on the smallest signal amplitude) and use a round continuously neutral density filter to control the power. The impinging laser power P is measured by using an ultraviolet-extended ultra-sensitive photodiode, where we record the power P before and after one single TA measurement and take the average value of these two. It has to be noted that since the ~3.4 eV signal is at the red-edge limit of our detection, we did not get as many data points as those of the ~3.8 eV signal because of a poor signal-to-noise ratio; nevertheless, it clearly shows a linear relationship between the signal amplitude and pump fluences at this band.

Because the LSPR band shifts between Au/SiO_2 and Au/TiO_2 in the steady-state absorption spectra (Fig. 1), when comparing the TA response of these two, a calibration of the actual excitation intensity needs to be performed. The broadband pump pulse covers the 2.0–2.4 eV region; thus we calculate the area below the absorption curve with respect to the background in this region, and obtain a ratio of Au/SiO_2:Au/TiO_2 ~ 1.3 of the absorption. Therefore, when plotting the TA results of the Au/SiO_2 and Au/TiO_2, a factor of 1.3 was multiplied in the case of Au/TiO_2.

APPENDIX D: ESTIMATION OF THE TPA ENHANCEMENT FACTOR

The rate of TPA is defined as [47]

$$\frac{dI_0}{dz} = -\beta I_0^2, \tag{D1}$$

where I_0 is the laser beam intensity, z is the direction of light propagation, and β is the TPA coefficient in cm/W. In the regime of TPA, a quadratic dependence on the laser intensity I_0 appears. The light intensity versus propagation distance becomes

$$I = \frac{I_0}{1+\beta l I_0}. \tag{D2}$$

I is the intensity of light transmitted through a path length l at a particular wavelength λ, and I_0 is the incident light intensity. Thus, the decrease in transmissivity along a path length l in the z direction is given by

$$T = \frac{I}{I_0} = \frac{1}{1+\beta l I_0}. \tag{D3}$$

Therefore, the induced TA signal can be written as

$$\Delta A = A - A_0 = \lg\frac{I_0}{I} = \lg\frac{1+\beta l I_0}{1}. \tag{D4}$$

According to the experimental and theoretical TPA coefficient of titanium dioxide single crystal (rutile), β is 18.6 ± 4.4 cm/GW at 532 nm for $c\|E$ configuration; β is 14.8 ± 42.9 cm/GW at 532 nm for $c\perp E$ configuration [48]. Even if Yuichi *et al.* obtained the β of titanium dioxide with rutile structure, there would not be orders of magnitude difference between anatase and rutile in the visible spectral region. Here, we take 15 cm/GW to simplify the calculation. The optical path length l equals the thickness of the flow cell: 0.2 mm. The incident light intensity $I_0 = \frac{P}{\pi r^2}$, where we take a power P of 5 mW and a Gaussian laser beam radius r of 100 μm. After adding an enhancement factor n, we obtain

$$\Delta A \approx \lg \frac{1 + n \cdot 6 \cdot 10^{-9}}{1}. \quad \textbf{(D5)}$$

Hence,

(1) in pure TiO_2 ($n = 1$), $\Delta A \approx 0$, the two-photon process is negligible;
(2) when the enhancement factor $n = 10^9$, $\Delta A \approx 0.85$;
(3) when the enhancement factor $n = 10^8$, $\Delta A \approx 0.20$;
(4) when the enhancement factor $n = 10^7$, $\Delta A \approx 0.03$.

Funding. Horizon 2020 European Research Council Advanced Grant (DYNAMOX); Schweizerischer Nationalfonds zur Förderung der Wissenschaftlichen Forschung (NCCR: MUST); China Scholarship Council.

Acknowledgment. The authors thank Dr. L. Mewes, Dr. M. Puppin, and B. Bauer for helpful discussions. L.W. acknowledges support from the China Scholarship Council (CSC).

Disclosures. The authors declare no conflicts of interest.

Data Availability. Data underlying the results presented in this paper are not publicly available at this time but may be obtained from the authors upon reasonable request.

REFERENCES

1. H. Long, A. Chen, G. Yang, Y. Li, and P. Lu, "Third-order optical nonlinearities in anatase and rutile TiO_2 thin films," Thin Solid Films **517**, 5601–5604 (2009).
2. E. Portuondo-Campa, A. Tortschanoff, F. van Mourik, and M. Chergui, "Ultrafast nonresonant response of TiO_2 nanostructured films," J. Chem. Phys. **128**, 244718 (2008).
3. D. Ji, J. Jang, J. H. Park, D. Kim, Y. S. Rim, D. K. Hwang, and Y.-Y. Noh, "Recent progress in the development of backplane thin film transistors for information displays," J. Inf. Disp. **22**, 1–11 (2021).
4. I. Becerril-Romero, D. Sylla, M. Placidi, Y. Sánchez, J. Andrade-Arvizu, V. Izquierdo-Roca, M. Guc, A. Pérez-Rodríguez, S. Grini, and L. Vines, "Transition-metal oxides for kesterite solar cells developed on transparent substrates," ACS Appl. Mater. Interfaces **12**, 33656–33669 (2020).
5. C. Guillen and J. Herrero, "Transparent electrodes based on metal and metal oxide stacked layers grown at room temperature on polymer substrate," Phys. Solidi A **207**, 1563–1567 (2010).
6. E. Baldini, L. Chiodo, A. Dominguez, M. Palummo, S. Moser, M. Yazdi-Rizi, G. Auböck, B. P. Mallett, H. Berger, and A. Magrez, "Strongly bound excitons in anatase TiO_2 single crystals and nanoparticles," Nat. Commun. **8**, 13 (2017).
7. E. Baldini, T. Palmieri, A. Dominguez, A. Rubio, and M. Chergui, "Giant exciton mott density in anatase TiO_2," Phys. Rev. Lett. **125**, 116403 (2020).
8. K. Iliopoulos, G. Kalogerakis, D. Vernardou, N. Katsarakis, E. Koudoumas, and S. Couris, "Nonlinear optical response of titanium oxide nanostructured thin films," Thin Solid Films **518**, 1174–1176 (2009).
9. H. B. Liao, R. F. Xiao, H. Wang, K. S. Wong, and G. K. L. Wong, "Large third-order optical nonlinearity in Au:TiO_2 composite films measured on a femtosecond time scale," Appl. Phys. Lett. **72**, 1817–1819 (1998).
10. P. Xiao-Niu, L. Min, Y. Liao, Z. Xian, and Z. Li, "Annealing induced aggregations and sign alterations of nonlinear absorption and refraction of dense Au nanoparticles in TiO_2 films," Chin. Phys. Lett. **25**, 4171–4173 (2008).
11. C. Sciancalepore, T. Cassano, M. L. Curri, D. Mecerreyes, A. Valentini, A. Agostiano, R. Tommasi, and M. Striccoli, "TiO_2 nanorods/PMMA copolymer-based nanocomposites: highly homogeneous linear and nonlinear optical material," Nanotechnology **19**, 205705 (2008).
12. M. H. Rittmann-Frank, C. J. Milne, J. Rittmann, M. Reinhard, T. J. Penfold, and M. Chergui, "Mapping of the photoinduced electron traps in TiO_2 by picosecond X-ray absorption spectroscopy," Angew. Chem. Int. Ed. **53**, 5858–5862 (2014).
13. E. Baldini, T. Palmieri, T. Rossi, M. Oppermann, E. Pomarico, G. Auböck, and M. Chergui, "Interfacial electron injection probed by a substrate-specific excitonic signature," J. Am. Chem. Soc. **139**, 11584–11589 (2017).
14. Z. K. Zhou, M. Li, X. R. Su, Y. Y. Zhai, H. Song, J. B. Han, and Z. H. Hao, "Enhancement of nonlinear optical properties of Au–TiO_2 granular composite with high percolation threshold," Phys. Solidi A **205**, 345–349 (2008).
15. M. Kyoung and M. Lee, "Z-scan studies on the third-order optical nonlinearity of Au nanoparticles embedded in TiO_2," Bull. Korean Chem. Soc. **21**, 26–28 (2000).
16. M. Anija, J. Thomas, N. Singh, A. Sreekumaran Nair, R. T. Tom, T. Pradeep, and R. Philip, "Nonlinear light transmission through oxide-protected Au and Ag nanoparticles: an investigation in the nanosecond domain," Chem. Phys. Lett. **380**, 223–229 (2003).
17. S. Linic, P. Christopher, and D. B. Ingram, "Plasmonic-metal nanostructures for efficient conversion of solar to chemical energy," Nat. Mater. **10**, 911–921 (2011).
18. A. Furube, L. Du, K. Hara, R. Katoh, and M. Tachiya, "Ultrafast plasmon-induced electron transfer from gold nanodots into TiO_2 nanoparticles," J. Am. Chem. Soc. **129**, 14852–14853 (2007).
19. L. Du, A. Furube, K. Yamamoto, K. Hara, R. Katoh, and M. Tachiya, "Plasmon-induced charge separation and recombination dynamics in gold-TiO_2 nanoparticle systems: dependence on TiO_2 particle size," J. Phys. Chem. C **113**, 6454–6462 (2009).
20. J. Sá, P. Friedli, R. Geiger, P. Lerch, M. H. Rittmann-Frank, C. J. Milne, J. Szlachetko, F. G. Santomauro, J. A. van Bokhoven, M. Chergui, M. J. Rossi, and H. Sigg, "Transient mid-IR study of electron dynamics in TiO_2 conduction band," Analyst **138**, 1966–1970 (2013).
21. L. Du, A. Furube, K. Hara, R. Katoh, and M. Tachiya, "Ultrafast plasmon induced electron injection mechanism in gold–TiO_2 nanoparticle system," J. Photochem. Photobiol. C **15**, 21–30 (2013).
22. C. Clavero, "Plasmon-induced hot-electron generation at nanoparticle/metal-oxide interfaces for photovoltaic and photocatalytic devices," Nat. Photonics **8**, 95–103 (2014).
23. D. C. Ratchford, A. D. Dunkelberger, I. Vurgaftman, J. C. Owrutsky, and P. E. Pehrsson, "Quantification of efficient plasmonic hot-electron injection in gold nanoparticle–TiO_2 films," Nano Lett. **17**, 6047–6055 (2017).
24. L. Du, X. Shi, G. Zhang, and A. Furube, "Plasmon induced charge transfer mechanism in gold-TiO_2 nanoparticle systems: the size effect of gold nanoparticle," J. Appl. Phys. **128**, 213104 (2020).
25. L. Amidani, A. Naldoni, M. Malvestuto, M. Marelli, P. Glatzel, V. Dal Santo, and F. Boscherini, "Probing long-lived plasmonic-generated charges in TiO_2/Au by high-resolution X-ray absorption spectroscopy," Angew. Chem. Int. Ed. **54**, 5413–5416 (2015).
26. S. K. Cushing, C.-J. Chen, C. L. Dong, X.-T. Kong, A. O. Govorov, R.-S. Liu, and N. Wu, "Tunable nonthermal distribution of hot electrons in a semiconductor injected from a plasmonic gold nanostructure," ACS Nano **12**, 7117–7126 (2018).
27. M. Borgwardt, J. Mahl, F. Roth, L. Wenthaus, F. Braußе, M. Blum, K. Schwarzburg, G. Liu, F. M. Toma, and O. Gessner, "Photoinduced charge carrier dynamics and electron injection efficiencies in Au nanoparticle-sensitized TiO_2 determined with picosecond time-resolved X-ray photoelectron spectroscopy," J. Phys. Chem. Lett. **11**, 5476–5481 (2020).
28. E. Baldini, T. Palmieri, E. Pomarico, G. Auböck, and M. Chergui, "Clocking the ultrafast electron cooling in anatase titanium dioxide nanoparticles," ACS Photon. **5**, 1241–1249 (2018).
29. L. Wang, T. Rossi, M. Oppermann, B. Bauer, L. Mewes, D. Zare, T. H. Chow, J. Wang, and M. Chergui, "Slow charge carrier relaxation in gold nanoparticles," J. Phys. Chem. C **124**, 24322–24330 (2020).
30. L. Wang, D. Zare, T. H. Chow, J. Wang, M. Magnozzi, and M. Chergui, "Disentangling light- and temperature-induced thermal effects in colloidal Au nanoparticles," J. Phys. Chem. C **126**, 3591–3599 (2022).

31. L. Wang, M. Oppermann, M. Puppin, B. Bauer, T. H. Chow, J. Wang, and M. Chergui, "Interband transition probing of coherent acoustic phonons of gold/metal oxide core–shell nanoparticles," Appl. Phys. Lett. **122**, 082201 (2023).
32. G.-Y. Yao, Q.-L. Liu, and Z.-Y. Zhao, "Studied localized surface plasmon resonance effects of Au nanoparticles on TiO_2 by FDTD simulations," Catalysts **8**, 236 (2018).
33. Y. Hattori, S. Gutiérrez Álvarez, J. Meng, K. Zheng, and J. Sá, "Role of the metal oxide electron acceptor on gold–plasmon hot-carrier dynamics and its implication to photocatalysis and photovoltaics," ACS Appl. Nano Mater. **4**, 2052–2060 (2021).
34. E. Le Ru and P. Etchegoin, *Principles of Surface-Enhanced Raman Spectroscopy* (Elsevier, 2008).
35. Y. Fang, N.-H. Seong, and D. D. Dlott, "Measurement of the distribution of site enhancements in surface-enhanced Raman scattering," Science **321**, 388–392 (2008).
36. M. A. El-Sayed, "Some interesting properties of metals confined in time and nanometer space of different shapes," Acc. Chem. Res. **34**, 257–264 (2001).
37. M. B. Mohamed, V. Volkov, S. Link, and M. A. El-Sayed, "The 'lightning' gold nanorods: fluorescence enhancement of over a million compared to the gold metal," Chem. Phys. Lett. **317**, 517–523 (2000).
38. S. M. Morton, D. W. Silverstein, and L. Jensen, "Theoretical studies of plasmonics using electronic structure methods," Chem. Rev. **111**, 3962–3994 (2011).
39. Z. Hu and L. Jensen, "A discrete interaction model/quantum mechanical method for simulating plasmon-enhanced two-photon absorption," J. Chem. Theory Comput. **14**, 5896–5903 (2018).
40. Q. Ruan, L. Shao, Y. Shu, J. Wang, and H. Wu, "Growth of monodisperse gold nanospheres with diameters from 20 nm to 220 nm and their core/satellite nanostructures," Adv. Opt. Mater. **2**, 65–73 (2014).
41. C. Fang, H. Jia, S. Chang, Q. Ruan, P. Wang, T. Chen, and J. Wang, "(Gold core)/(titania shell) nanostructures for plasmon-enhanced photon harvesting and generation of reactive oxygen species," Energy Environ. Sci. **7**, 3431–3438 (2014).
42. G. Auböck, C. Consani, R. Monni, A. Cannizzo, F. van Mourik, and M. Chergui, "Femtosecond pump/supercontinuum-probe setup with 20 kHz repetition rate," Rev. Sci. Instrum. **83**, 093105 (2012).
43. G. Auböck, C. Consani, F. van Mourik, and M. Chergui, "Ultrabroadband femtosecond two-dimensional ultraviolet transient absorption," Opt. Lett. **37**, 2337–2339 (2012).
44. P. Baum, S. Lochbrunner, and E. Riedle, "Zero-additional-phase SPIDER: full characterization of visible and sub-20-fs ultraviolet pulses," Opt. Lett. **29**, 210–212 (2004).
45. J. Mooney and P. Kambhampati, "Get the basics right: Jacobian conversion of wavelength and energy scales for quantitative analysis of emission spectra," J. Phys. Chem. Lett. **4**, 3316–3318 (2013).
46. C. Slavov, H. Hartmann, and J. Wachtveitl, "Implementation and evaluation of data analysis strategies for time-resolved optical spectroscopy," Anal. Chem. **87**, 2328–2336 (2015).
47. P. Prabhakaran, T. D. Kim, and K. S. Lee, "8.09-polymer photonics," in *Polymer Science: A Comprehensive Reference*, K. Matyjaszewski and M. Möller, eds. (Elsevier, 2012), pp. 211–260.
48. Y. Watanabe, M. Ohnishi, and T. Tsuchiya, "Measurement of nonlinear absorption and refraction in titanium dioxide single crystal by using a phase distortion method," Appl. Phys. Lett. **66**, 3431–3432 (1995).